Fast Site-to-site Electron Transfer of High-entropy Alloy Nanocatalyst Driving Redox Electrocatalysis

Hongdong Li
Qingdao University of Science and Technology
Yi Han
Qingdao University of Science and Technology
Huan Zhao
Qingdao University of Science and Technology
Wenjing Qi
Chongqing Normal University
Dan Zhang
Qingdao University of Science and Technology
Yaodong Yu
Qingdao University of Science and Technology
Wenwen Cai
Qingdao University of Science and Technology
Shaoxiang Li
Qingdao University of Science and Technology
Jianping Lai
Qingdao University of Science and Technology
Bolong Huang
Hong Kong Polytechnic University https://orcid.org/0000-0002-2526-2002
Lei Wang (inorchemwl@126.com)
Qingdao University of Science and Technology

Article

Keywords: electrocatalysts, high-entropy alloys, hydrogen evolution reaction, methanol oxidation reaction

Posted Date: August 1st, 2020

DOI: https://doi.org/10.21203/rs.3.rs-48124/v1

Version of Record: A version of this preprint was published at Nature Communications on October 28th, 2020. See the published version at https://doi.org/10.1038/s41467-020-19277-9.

Abstract

Designing electrocatalysts with high-performance for both reduction and oxidation reactions faces severe challenges. Here, the uniform and small size (~3.4 nm) high-entropy alloys (HEAs) Pt18Ni26Fe15Co14Cu27 nanoparticles (NPs) are synthesized by a simple low-temperature (<250 oC) oil phase synthesis strategy at atmospheric pressure for the first time. The Pt18Ni26Fe15Co14Cu27/C catalyst exhibits excellent electrocatalytic performance for hydrogen evolution reaction (HER) and methanol oxidation reaction (MOR). The catalyst is one of the best performance achieved by state-of-the-art alkaline HER catalysts, which shows an ultrasmall overpotential of 11 mV at the current density of 10 mA cm-2, excellent activity (10.96 A mg-1Pt at -0.07 V vs. reversible hydrogen electrode) and stability in the alkaline medium. Furthermore, it is also the most efficient catalyst (15.04 A mg-1Pt) ever reported for MOR in alkaline solution. DFT calculations confirm the multi-active sites for both HER and MOR on the HEA surface as the key factor for both proton and intermediate transformation. Meanwhile, the construction of HEA surfaces supplies the fast site-to-site electron transfer for both reduction and oxidation processes.

Introduction

Electrocatalytic processes play a vital role in energy conversion and reducing the environmental pollution.[1-5] To improve the activity, selectivity, and stability of the catalytic reaction, it is necessary to develop high-performance advanced catalysts that can meet the needs of rapid development.[6-12]

High-entropy alloys (HEAs) have attracted wide interest as catalytic materials in the past few years.[13-16] The alloy contains five or more elements which have similar atomic ratios.[16,17] The atomic size of each component is different, which can cause lattice distortion.[18] Besides, the presence of multiple components is conducive to promoting the formation of solid solution phase and inhibiting the movement of dislocations. These characteristics of HEA lead to some unique characteristics, such as strong fracture toughness, corrosion resistance and high mechanical strength.[19-21] In catalysis field, the adsorption of molecules and intermediates species on the surface of the catalyst affects the catalytic activity.[13,22] These adsorption energies can be adjusted by alloying as compared to pure elements to increase catalytic activity.[23-25] Recently, some HEAs had used as catalysts for electrocatalytic reactions, which display superior stability and catalytic selectivity and activity compared with traditional alloys.[13,26-30] However, the traditional method mainly produce bulk HEAs rather than nanostructures.[26,31-34] Moreover, the preparation of uniform nanostructured HEAs with small size (< 10 nm) currently requires specific equipment (fast heating/cooling rate, ~10^5 K per second), high temperature (~2000 kelvin), and high temperature resistant and conductive substrate (carbon nanofiber), such as carbon-thermal shock method. [35]

In this work, we synthesized the small size (~3.4 nm) and uniform HEA $Pt_{18}Ni_{26}Fe_{15}Co_{14}Cu_{27}$ nanoparticles (NPs) by a simple low-temperature oil phase synthesis method at atmospheric pressure.

The $Pt_{18}Ni_{26}Fe_{15}Co_{14}Cu_{27}$/C catalyst displayed a low overpotential (11 mV at 10 mA cm^{-2}), the superior activity of 10.96 A mg^{-1}_{Pt} at -0.07 V *vs.* reversible hydrogen electrode (RHE) for HER (reduction reaction) in 1 M KOH solution (one of the best performances achieved in the alkaline HER catalyst, **Supplementary Table 2**), and through the chronoamperometric method and 10000^{th} CV tests, it indicates that the notable stability of the HEA catalyst. We further also measured the electrocatalytic activity of $Pt_{18}Ni_{26}Fe_{15}Co_{14}Cu_{27}$/C for MOR (oxidation reaction) at 1M KOH+1M CH_3OH electrolyte, it also exhibited an oustanding activity (15.04 A mg^{-1}_{Pt}), and it has the highest alkaline MOR activity among ever reported (**Supplementary Table 3**). Theoretical calculations revealed that each element in HEA display different contributions for the electrocatalysis process, which promotes the site-to-site electron transfer and the stabilization of the intermediates. HEA showed the multi-active sites for both HER and MOR for achieving superior performance and stability.

Results And Discussion

Synthesis and characterization of PtNiFeCoCu HEA NPs. PtNiFeCoCu HEA NPs were prepared through a simple one-pot oil phase synthesis method at 220 °C for 2 h. The inductively coupled plasma atomic emission spectroscopy (ICP-AES) result shows that the atomic ratio of Pt, Ni, Fe, Co, and Cu was 18:26:15:14:27 (**Supplementary Table 1**), the prepared NPs-HEA was named $Pt_{18}Ni_{26}Fe_{15}Co_{14}Cu_{27}$. As shown in Fig. 1a and **b**, the transmission electron microscopy (TEM) images of $Pt_{18}Ni_{26}Fe_{15}Co_{14}Cu_{27}$ NPs display the morphology is uniform, and the diameter of $Pt_{18}Ni_{26}Fe_{15}Co_{14}Cu_{27}$ NPs is about 3.39 ± 0.59 nm (the inset in Fig. 1a). The high-resolution TEM (HRTEM) (Fig. 1c) image of $Pt_{18}Ni_{26}Fe_{15}Co_{14}Cu_{27}$ NPs exhibits that the lattice spacing is 0.218 nm, corresponding to the (111) facet. The powder X-ray diffraction (PXRD) pattern (**Supplementary Fig. 1a**) suggests the fcc structure of the NPs-HEAs, the two peaks at around 41.1^o and 47.8^o, which can be assigned to the (111) and (200) facets. The position of the broad diffraction peak is significant shift compared with the diffraction peaks of pure Pt, Ni, Fe, Co, and Cu (**Supplementary Fig. 1b**), it shows that these elements have been introduced into the nanostructure to form HEAs structure. Figure 1d shows the elemental maps of NPs-HEAs, Pt, Ni, Fe, Co and Cu elements are uniformly distributed in the HEA nanostructure.

The X-ray photoelectron spectroscopy (XPS) of $Pt_{18}Ni_{26}Fe_{15}Co_{14}Cu_{27}$ NPs were tested, it also shows the presence of these Pt, Ni, Fe, Co, and Cu elements (**Supplementary Fig. 2a**), the atomic ratio of Pt, Ni, Fe, Co, and Cu was 21.2:27.4:15.2:13.7:22.5, further proving that the HEA was successfully prepared. As shown in **Supplementary Fig. 2b**, the Pt $4f_{7/2}$ and Pt $4f_{5/2}$ peaks are located at 71.3 and 74.7 eV, respectively. Pt mainly exists in the form of zero valences and a small amount of 2 + valence.[29] The Ni 2p spectra display the coexistence of Ni^0 (852.8 eV) and Ni^{2+} (855.6 eV) and a satellite peak locate at 861.6 eV (**Supplementary Fig. 2c**), the content of Ni^0 is lower than the content of Ni^{2+} because of the high chemical activity of Ni.[28,29] The Fe 2p spectra in **Supplementary Fig. 2d** shows two peaks at 711.6 eV and 724.8 eV, which can be attributed to Fe $2p_{3/2}$ and Fe $2p_{1/2}$, respectively. The two Co 2p peaks can be

assigned to Co $2p_{3/2}$ (780.8 eV) and Co $2p_{1/2}$ (797.0 eV) (**Supplementary Fig. 2e**). The Cu 2p spectra (**Supplementary Fig. 2f**) also exhibits Cu^0 (931.7 eV) and Cu^{2+} (933.5 eV) peaks coexist in the sample.

Electrocatalytic properties of $Pt_{18}Ni_{26}Fe_{15}Co_{14}Cu_{27}$/C towards HER. The HER (reduction reaction) activity and stability of the $Pt_{18}Ni_{26}Fe_{15}Co_{14}Cu_{27}$/C catalyst were investigated by a series of electrochemical tests and compared with commercial Pt/C. Figure 2a shows the CV curves of $Pt_{18}Ni_{26}Fe_{15}Co_{14}Cu_{27}$/C and commercial Pt/C catalysts in N_2-saturated 1 M KOH at a scan rate of 20 mV s^{-1}. After activation, the linear sweep voltammetry (LSV) curve of the $Pt_{18}Ni_{26}Fe_{15}Co_{14}Cu_{27}$/C catalyst displays a low overpotential of 11 mV at the current density of 10 mA cm^{-2} (normalized to the electrode area), which is far superior to commercial Pt/C catalyst (84 mV) (Fig. 2b). As shown in Fig. 2b and Fig. 2d, the area activity (normalized to the geometric area) of NPs-HEAs $Pt_{18}Ni_{26}Fe_{15}Co_{14}Cu_{27}$/C catalyst reaches 83.78 mA cm^{-2} at -0.07 V *vs.* RHE, far more than area activity of commercial Pt/C catalyst (8.42 mA cm^{-2} at -0.07 V *vs.* RHE). From the Fig. 2c (LSV curves, normalized to the Pt mass), the mass activity for commercial Pt/C catalyst and $Pt_{18}Ni_{26}Fe_{15}Co_{14}Cu_{27}$/C catalyst are 0.83 A mg^{-1}_{Pt} and 10.96 A mg^{-1}_{Pt} at -0.07 V *vs.* RHE (Fig. 2d), respectively. And the $Pt_{18}Ni_{26}Fe_{15}Co_{14}Cu_{27}$/C catalyst also exhibits the superior HER performance in alkaline medium among the reported Pt-based catalysts and HEAs catalysts (**Supplementary Table 2**). As shown in Fig. 2e, the Tafel slopes of $Pt_{18}Ni_{26}Fe_{15}Co_{14}Cu_{27}$/C and Pt/C are 30 mV dec^{-1} and 98 mV dec^{-1}, respectively, which demonstrate that the HEAs catalyst greatly boosts HER kinetics.

To better understand the outstanding HER performance of the $Pt_{18}Ni_{26}Fe_{15}Co_{14}Cu_{27}$/C catalyst, we tested the electrochemical double-layer capacitance, electrochemical impedance spectra and turnover frequency (TOF). We found that the electrochemical double-layer capacitance of $Pt_{18}Ni_{26}Fe_{15}Co_{14}Cu_{27}$/C catalyst is higher than that of commercial Pt/C catalyst (**Supplementary Fig. 3**), indicating that the NPs-HEAs can expose more active sites. Also, electrochemical impedance spectra (**Supplementary Fig. 4**) exhibits $Pt_{18}Ni_{26}Fe_{15}Co_{14}Cu_{27}$/C catalyst has a smaller semicircular diameter than commercial Pt/C catalyst, the transfer resistance of $Pt_{18}Ni_{26}Fe_{15}Co_{14}Cu_{27}$/C is much lower than that of commercial Pt/C catalysts, indicating higher interfacial charge transfer rate and faster HER kinetics. The TOF value is used to characterize the activity of each site in the catalyst[36]. It is found that the TOF value of the $Pt_{18}Ni_{26}Fe_{15}Co_{14}Cu_{27}$/C catalyst is higher than Pt/C catalyst under various potentials (**Supplementary Fig. 6**), which shows the faster HER kinetics of $Pt_{18}Ni_{26}Fe_{15}Co_{14}Cu_{27}$/C catalyst. These results further indicate that the NPs-HEAs can improve the catalytic activity effectively.

The stability of the catalysts was checked using the chronoamperometric method and 10000th CV in 1.0 M KOH solution. The stability of the $Pt_{18}Ni_{26}Fe_{15}Co_{14}Cu_{27}$/C and Pt/C catalysts were measured at an overpotential of 11 mV and 84 mV (under current density 10 mA cm^{-2} condition, **Supplementary Fig. 7**), respectively. After 10 h test, 99% of the current density is maintained for the $Pt_{18}Ni_{26}Fe_{15}Co_{14}Cu_{27}$/C catalyst, while the current density of the Pt/C catalyst is only kept about 53%. To further evaluate the stability of $Pt_{18}Ni_{26}Fe_{15}Co_{14}Cu_{27}$/C and Pt/C catalysts, the 1000th and 10000th CV cycles in 1 M KOH

solution were performed. Figure 2f displays the LSV curves of $Pt_{18}Ni_{26}Fe_{15}Co_{14}Cu_{27}$/C catalyst before and after 1000th and 10000th CV cycles. There is no obvious negative shift at the current density of 10 mA cm^{-2}, exhibiting higher stability than Pt/C catalyst (**Supplementary Fig. 8**, a negative shift of ~33 mV at 10 mA cm^{-2} after 10000th CV cycles). In addition, the morphology (**Supplementary Fig. 9**), the atomic ratio (**Supplementary Table 1**), lattice spacing and the XRD peaks (**Supplementary Fig. 10**) of catalyst did not change significantly after the stability test. These results further suggest the excellent stability of the $Pt_{18}Ni_{26}Fe_{15}Co_{14}Cu_{27}$/C catalyst.

Electrocatalytic properties of $Pt_{18}Ni_{26}Fe_{15}Co_{14}Cu_{27}$/C towards MOR. To further explore the $Pt_{18}Ni_{26}Fe_{15}Co_{14}Cu_{27}$/C catalyst as redox bi-function electrocatalysts, we tested the MOR (oxidation reaction) activity. As shown in Fig. 3a and **Supplementary Fig. 11**, the $Pt_{18}Ni_{26}Fe_{15}Co_{14}Cu_{27}$/C catalyst shows higher activity compared to Pt/C catalyst for MOR in 1 M KOH + 1 M CH_3OH electrolyte at a sweep rate of 20 mV s^{-1}. And an onset potential (the mass activity of 0.1 A mg^{-1}_{pt}) was observed to decrease by 133 mV in the $Pt_{18}Ni_{26}Fe_{15}Co_{14}Cu_{27}$/C catalyst compared to the Pt/C catalyst (the inset of Fig. 3a), indicating that the activation barrier of methanol oxidation is lower. The $Pt_{18}Ni_{26}Fe_{15}Co_{14}Cu_{27}$/C catalyst achieves 10 times (4 times) higher in mass activity and area activity (15.04 A mg^{-1}_{pt}, 114.93 mA cm^{-2}) than that of Pt/C catalyst (1.45 A mg^{-1}_{pt}, 27.48 mA cm^{-2}) at peak potential for MOR (Fig. 3b). Moreover, among recently reported the Pt-based materials for MOR in alkaline medium, the $Pt_{18}Ni_{26}Fe_{15}Co_{14}Cu_{27}$/C catalyst exhibits the highest mass activity (**Supplementary Table 3**).

To study the stability of the $Pt_{18}Ni_{26}Fe_{15}Co_{14}Cu_{27}$/C and Pt/C catalysts in MOR, the chronoamperometry test at 0.65 V *vs.* RHE and 1000 CV cycles were executed. After 5000s chronoamperometry test (Fig. 3c), the $Pt_{18}Ni_{26}Fe_{15}Co_{14}Cu_{27}$/C (3.79 A mg^{-1}_{pt}) catalyst shows higher stability than that of commercial Pt/C (0.20 A mg^{-1}_{pt}). After 1000 CV cycles, the mass activity of the $Pt_{18}Ni_{26}Fe_{15}Co_{14}Cu_{27}$/C and Pt/C catalysts decay by about 6.4% and 26.9% (Fig. 3d and **Supplementary Figs. 12**), further confirmed the excellent stability of $Pt_{18}Ni_{26}Fe_{15}Co_{14}Cu_{27}$/C catalyst. And the morphology and element ratio of $Pt_{18}Ni_{26}Fe_{15}Co_{14}Cu_{27}$/C catalyst did not obvious change after stability test (**Supplementary Fig. 13, Supplementary Table 1**). These test results indicate that NPs-HEAs catalyst achieves double enhancement of catalytic activity and stability.

In MOR, the main route for catalyst deactivation is the poisoning effect of CO intermediates.[37–39] The I_f/I_b (I_f: forward current density, I_b: backward current density) ratio of $Pt_{18}Ni_{26}Fe_{15}Co_{14}Cu_{27}$/C catalyst (3.26) is larger than that of Pt/C (2.31), which shows the strong CO anti-poisoning performance of $Pt_{18}Ni_{26}Fe_{15}Co_{14}Cu_{27}$/C catalyst. And from CO stripping curves (**Supplementary Fig. 14**), the onset potentials of the $Pt_{18}Ni_{26}Fe_{15}Co_{14}Cu_{27}$/C (0.391 V *vs.* RHE) display a 181 mV decrease compared with Pt/C (0.572 V *vs.* RHE) catalyst. It further shows that the $Pt_{18}Ni_{26}Fe_{15}Co_{14}Cu_{27}$/C catalyst has better CO anti-poisoning performance.

DFT studies. We applied DFT calculations to explore the HER and MOR performances in HEA. The HEA structure has been constructed in which all the elements were distributed randomly and the slightly Ni and Cu rich features for the surface (Fig. 4a). From the side view, the lattice has shown a highly stable structure, in which the lattice shows subtle distortion after relaxation, which indicates good durability for electrocatalysis. Meanwhile, the surface Ni and Co dominate the electroactive region near the Fermi level (E_F) (Fig. 4b). To further understand the electronic structures, the partial projected density of states (PDOSs) of each element in HEA has been illustrated. Notably, Pt-5d occupies the deepest position near E_V -4.5 eV (EV = 0 eV), playing as the electron reservoir for reduction process such as HER. Both Co-3d and Ni-3d orbitals dominate the bands near E_F, which locate at E_V -1.0 eV, contributing to the electron depletion center for HER and MOR. Moreover, the 3d orbitals of Cu, Co, and Fe not only alleviate the energy barrier of dual-way electron transfer for oxidation and reduction process but also facilitate the stabilization of intermediates for MOR (Fig. 4c). A detailed study of the site-dependent PDOSs of each element was illustrated (Fig. 4d). Notably, only the surface Pt demonstrates an evident upshift towards the E_F, which promotes the electron transfer for the HEA surfaces. Fe shows a site-independent electronic structure within HEA, which preserves the stable adsorption of intermediates with stronger anti-poisoning capability for the MOR process. From the bulk structure to the surface site, Co sites display an alleviation of the e_g-t_{2g} splitting effect, supporting an enhanced electron transfer efficiency for electrocatalysis. Both Ni exhibits the relatively stable d-band-center to maintain the electroactive electron boosting center. For Cu sites closer to the surface, the 3d orbitals show a slight upshift trend to support the electroactivity of the HEA. Thus, the synergistic effect of multi-active sites on the HEA surface determines the remarkable performance of HER and MOR (Fig. 4d). For the HER process, the initial adsorption of water determines the efficiency of water-splitting and the following proton transfer. For the water adsorption process, the evident downshift of *s,p* orbitals in H_2O has been noticed, which confirms the active electron transfer from the HEA to the water to achieve the stable adsorption and lays a good foundation for the following water dissociation (Fig. 4e). Similarly, we notice the adsorption of CH_3OH on HEA indicates the evident downshifting of *s,p* bands, and overlapping with electroactive d orbitals of the surface (Fig. 4f). For the multi-electron involved MOR process, the linear correlation of intermediates transformation is the key to guarantee the proton and electron transfer. Such a linear correlation is noticed for the *s,p*-orbitals of key intermediates along the MOR process, which not only supports the efficient oxidation of the intermediates but also leads to the optimal binding strength during the intermediate transformation. Thus, superior MOR performance is guaranteed in the HEA (Fig. 4g).

Then, we further interpret the reaction trend for both HER and MOR from both the structural configuration and energetic reaction pathways. The most stable structural configurations of four key initial reactants and intermediates have been displayed. The most stable adsorption of CH_3OH and H_2O locates near Ni and Fe sites, respectively. The OH is stabilized in the neighboring hollow sites, which avoids the active site blocking during both HER and MOR. Meanwhile, the H adsorption prefers the hollow site near Ni and Co, which is distinct from the OH. Thus, the multi-site adsorption for HER and MOR process on HEA guarantees superior performances (Fig. 5a). Moreover, we have supplied the adsorption sites mapping of the surface to support the HER mechanism (Fig. 5b). Notably, the different sites in HEA surfaces

demonstrated very varied adsorption preference for the intermediates. For HER, the initial adsorption of H_2O locates on the Fe sites, which activates the dissociation of water molecules and facilitates the stabilization of *OH in the neighboring hollow sites. Meanwhile, the nearby Ni, Co show the relatively preferred H* adsorption after the water dissociation, leading to the stabilization of H in the hollow sites surrounded by Co and Ni. The generated H_2 shows overall weak binding to the surface, indicating the quick desorption process to guarantee the efficient HER process. Therefore, our additional information has supplied the binding stability of the intermediates for the HER process, which supports the Volmer-Heyrovsky mechanism. The HER process supports a continuous downhill trend, confirming the efficient proton and electron transfer (Fig. 5c). Owing to the multi-active sites for OH and H, the water-dissociation demonstrates a low activation barrier of 0.11 eV for the transition state (Fig. 5d). For the MOR process, the rate-determining step occurs at [CHO*+ 3*OH + 3H_2O] to [HCOOH + 2*OH + 4H_2O] with the largest energy barrier of 0.45 eV. The transition state displays the activation energy of 0.64 eV. The overall MOR process is exothermic, which releases 2.34 eV energy (Fig. 5e). The anti-poisoning capability is another essential requirement for the long-term application of MOR electrocatalysts. Compared to MOR, the formation of CO shows a much larger energy barrier of 0.81 eV and activation energy (0.94 eV), resulting in the suppression of the CO poisoning. The holistic reaction trend of the CO poisoning mechanism is also much weaker than the MOR process, which explains both the superior electroactivity and durability of the HEA (Fig. 5f).

Conclusion

In conclusion, we have synthesized the uniform and small size $Pt_{18}Ni_{26}Fe_{15}Co_{14}Cu_{27}$ nanoparticles high-entropy alloy nanoparticles by a simple low-temperature synthesis method at atmospheric pressure. Electrocatalytic test results showed that the obtained $Pt_{18}Ni_{26}Fe_{15}Co_{14}Cu_{27}$/C catalyst has excellent bi-functional electrocatalytic properties for reduction reaction (HER) and oxidation reaction (MOR). $Pt_{18}Ni_{26}Fe_{15}Co_{14}Cu_{27}$/C catalyst showed an ultrasmall overpotential (11 mV at 10 mA cm^{-2}) and superior activity (10.96 A mg^{-1}_{Pt} at -0.07 V *vs.* RHE) and stability for HER, which is one of the best HER activity in alkaline medium. And it is also the effective catalysts for MOR and displayed the excellent activity (15.04 A mg^{-1}_{Pt}) and better CO anti-poisoning in alkaline solution, which is the best alkaline MOR activity among the ever-reported. Through DFT calculations, the origin of remarkable electroactivity and durability of HEA in HER and MOR is attributed to the synergistic effect of each element for efficient electron transfer. The optimized electronic environment constructs the strategy of the multi-active site for adsorption and transformation of key intermediates, which maximizes the utilization of surface electroactivity. The simple oil phase synthesis strategy proposed in this work, as well as the multi-active sites and fast site-to-site electron transfer mechanism, which is expected to lay the foundation for the preparation of other high-entropy alloys and their application in related electrocatalysis.

Methods

Preparation of high-entropy alloy $Pt_{18}Ni_{26}Fe_{15}Co_{14}Cu_{27}$ Nanoparticles (NPs). CTAC (50 mg) was added into oleylamine (5 mL) in a vial. After sonication, $Pt(acac)_2$ (10 mg), $Ni(acac)_2$ (6.4 mg), $Fe(acac)_3$ (8.8 mg), $Co(acac)_3$ (8.9 mg), $Cu(acac)_2$ (6.5 mg), glucose (60 mg) and $Mo(CO)_6$ (33 mg) were added into the vial. In order to obtain a homogeneous solution, the mixture was sonicated for 1 h. The vial was heated to 220 ^oC and then kept 2 h under magnetic stirring. The black colloidal products were collected by centrifugation and washed two times with an ethanol/cyclohexane mixture. Finally, the black colloidal products were kept in cyclohexane for further use.

Characterization. The transmission electron microscopy (TEM) and high-resolution TEM (HRTEM) images of the samples were characterized by an FEI Tecnai-G2 F30 at an accelerating voltage of 300 KV. Powder X-ray diffraction (XRD) spectra was recorded on X'Pert-PRO MPD diffractometer operating at 40 KV and 40 mA with Cu Kα radiation. The compositions of the high-entropy alloy NPs were determined by the inductively coupled plasma atomic emission spectrometer (ICP-AES, Varian 710-ES). The catalysts after the durability tests were scratched off the glassy carbon electrode with the aid of sonication in ethanol and then collected for further TEM, XRD, and ICP characterization. The X-ray photoelectron spectra (XPS) of the sample was measured via a VG ESCALABMK II spectrometer.

Calculation Setup. For all the calculations within this work, we have applied the DFT calculations within CASTEP code[40]. The GGA and PBE exchange-correlation functionals are selected for all the calculations[41,42]. The cutoff energy of plane-wave basis sets based on the ultrasoft pseudopotential has been set to 440 eV with the selection of the algorithm Broyden-Fletcher-Goldfarb-Shannon (BFGS) for all the geometry optimizations[43]. To specifically discuss the electrocatalysis on the surface, we have applied the HEA model with similar stoichiometry as experimental characterizations. The HEA model has been built, which consists of 126 atoms in total. The atomic arrangements of different elements are constructed randomly by following the same ratio as the experiments of $Pt_{18}Ni_{26}Fe_{15}Co_{14}Cu_{27}$. Based on the components of the HEA by experimental characterizations, Ni and Cu have the highest concentration, which is 26% and 27%, respectively. To determine the most possible preferred model, we have compared the total energy of the HEA model with different surface arrangements, in which the present applied model with Cu and Ni slight rich feature has been the most stable one. Therefore, we have applied the HEA surface model with Cu and Ni rich feature. The reaction energy has been considered based on the intermediate adsorptions on the surface[34].

The Monkhost-Pack reciprocal space integration was performed using coarse k-points with a mesh of $2 \times 2 \times 1$[44], which was guided by the initial convergence test. With these settings, the overall total energy for each step is converged to less than 5.0×10^{-5} eV per atom. The Hellmann-Feynman forces on the atom were converged to less than 0.001 eV/Å.

Declarations

Author contributions

L.W. and J.L. conceived and supervised the research. J.L. and H.L. designed the experiments. H.L. performed most of the experiments and data analysis. B.H. performed the DFT calculations and mechanistic analysis. Y.H. and H.Z. prepared the electrodes and helped with electrochemical measurements. W.Q. and D.Z. conducted and analyzed HRTEM micrographs and mapping images. Y.Y. performed and analyzed XRD and ICP measurements. S.L. and W.C. analyzed XPS measurements. All authors discussed the results and commented on the manuscript.

Acknowledgment

This work was supported by the National Natural Science Foundation of China (21571112, 51572136, 51772162, 51802171), the Taishan Scholars Program, Natural Science Foundation of Shandong Province, China (ZR2018BB031), Open Fund of the Key Laboratory of Eco-chemical Engineering (Qingdao University of Science and Technology, No. KF1702), the Taishan Scholar Project of Shandong Province (tsqn201909123)

References

1. Glenk, G. & Reichelstein, S. Economics of converting renewable power to hydrogen. *Nat. Energy* **4**, 216–222 (2019).
2. Seh, Z. W. *et al.* Combining theory and experiment in electrocatalysis: Insights into materials design. *Science* **355**, 146–157 (2017).
3. Lai, J. & Guo, S. Design of ultrathin Pt-based multimetallic nanostructures for efficient oxygen reduction electrocatalysis. *Small* **13**, 1702156 (2017).
4. Yin, H. *et al.* 2D Electrocatalysts for converting earth-abundant simple molecules into value-added commodity chemicals: Recent progress and perspectives. *Adv. Mater.* **32**, 1904870 (2019).
5. Leow, W. R. *et al.* Chloride-mediated selective electrosynthesis of ethylene and propylene oxides at high current density. *Science* **368**, 1228 (2020).
6. Li, L., Wang, P., Shao, Q. & Huang, X. Metallic nanostructures with low dimensionality for electrochemical water splitting. *Chem. Soc. Rev.* **49**, 3072–3106 (2020).
7. Lai, J., Nsabimana, A., Luque, R. & Xu, G. 3D porous carbonaceous electrodes for electrocatalytic applications. *Joule* **2**, 76–93 (2018).
8. Xie, C. *et al.* Insight into the design of defect electrocatalysts: From electronic structure to adsorption energy. *Mater. Today* **31**, 47–68 (2019).
9. Jin, H. *et al.* Emerging two-dimensional nanomaterials for electrocatalysis. *Chem. Rev.* **118**, 6337–6408 (2018).
10. Chen, Y. *et al.* Phase engineering of nanomaterials. *Nat. Rev. Chem.* **4**, 243–256 (2020).
11. Tian, X., Lu, X. F., Xia, B. Y. & Lou, X. W. Advanced electrocatalysts for the oxygen reduction reaction in energy conversion technologies. *Joule* **4**, 45–68, (2020).

12. Yuan, Y. *et al.* Zirconium nitride catalysts surpass platinum for oxygen reduction. *Nat. Mater.* **19**, 282–286 (2020).
13. Batchelor, T. A. A. *et al.* High-entropy alloys as a discovery platform for electrocatalysis. *Joule* **3**, 834–845 (2019).
14. George, E. P., Raabe, D. & Ritchie, R. O. High-entropy alloys. *Nat. Rev. Mater.* **4**, 515–534 (2019).
15. Chen, P. C. *et al.* Polyelemental nanoparticle libraries. *Science* **352**, 1565–1569 (2016).
16. Koo, W. T., Millstone, J. E., Weiss, P. S. & Kim, I. D. The design and science of polyelemental nanoparticles. *ACS Nano* **14**, 6407–6413 (2020).
17. Miracle, D. B. & Senkov, O. N. A critical review of high entropy alloys and related concepts. *Acta Mater.* **122**, 448–511 (2017).
18. Huang, K. *et al.* Exploring the impact of atomic lattice deformation on oxygen evolution reactions based on a sub-5 nm pure face-centred cubic high-entropy alloy electrocatalyst. *J. Mater. Chem. A* **8**, 11938–11947 (2020).
19. Lei, Z. *et al.* Enhanced strength and ductility in a high-entropy alloy via ordered oxygen complexes. *Nature* **563**, 546–550 (2018).
20. Zhang, W., Liaw, P. K. & Zhang, Y. Science and technology in high-entropy alloys. *Sci. China Mater.* **61**, 2–22 (2018).
21. Yeh, J. W. *et al.* Nanostructured high-entropy alloys with multiple principal elements: Novel alloy design concepts and outcomes. *Adv. Eng. Mater.* **6**, 299–303 (2004).
22. Guo, C. *et al.* Intermediate modulation on noble metal hybridized to 2D metal-organic framework for accelerated water electrocatalysis. *Chem* **5**, 2429–2441 (2019).
23. Lv, F. *et al.* Ir-based alloy nanoflowers with optimized hydrogen binding energy as bifunctional electrocatalysts for overall water splitting. *Small Methods* **4**, 1900129 (2020).
24. Tian, X. *et al.* Engineering bunched Pt-Ni alloy nanocages for efficient oxygen reduction in practical fuel cells. *Science* **366**, 850–856 (2019).
25. Xiong, L. *et al.* Octahedral gold-silver nanoframes with rich crystalline defects for efficient methanol oxidation manifesting a CO-promoting effect. *Nat. Commun.* **10**, 3782 (2019).
26. Zhang, G. *et al.* High entropy alloy as a highly active and stable electrocatalyst for hydrogen evolution reaction. *Electrochim. Acta* **279**, 19–23 (2018).
27. Glasscott, M. W. *et al.* Electrosynthesis of high-entropy metallic glass nanoparticles for designer, multi-functional electrocatalysis. *Nat. Commun.* **10**, 2650 (2019).
28. Jin, Z. *et al.* Nanoporous Al-Ni-Co-Ir-Mo high-entropy alloy for record-high water splitting activity in acidic environments. *Small* **15**, 1904180 (2019).
29. Qiu, H. J. *et al.* Nanoporous high-entropy alloys for highly stable and efficient catalysts. *J. Mater. Chem. A* **7**, 6499–6506 (2019).
30. Xie, P. *et al.* Highly efficient decomposition of ammonia using high-entropy alloy catalysts. *Nat. Commun.* **10**, 4011 (2019).

31. Yao, C. Z. *et al.* Electrochemical preparation and magnetic study of Bi-Fe-Co-Ni-Mn high entropy alloy. *Electrochim. Acta* **53**, 8359–8365 (2008).
32. Soare, V. *et al.* Electrochemical deposition and microstructural characterization of AlCrFeMnNi and AlCrCuFeMnNi high entropy alloy thin films. *Appl. Surf. Sci.* **358**, 533–539 (2015).
33. Nellaiappan, S. *et al.* High-entropy alloys as catalysts for the CO_2 and CO reduction reactions: Experimental realization. *ACS Catal.* **10**, 3658–3663 (2020).
34. Pedersen, J. K., Batchelor, T. A. A., Bagger, A. & Rossmeisl, J. High-entropy alloys as catalysts for the CO_2 and CO reduction reactions. *ACS Catal.* **10**, 2169–2176 (2020).
35. Yao, Y. *et al.* Carbothermal shock synthesis of high-entropy-alloy nanoparticles. *Science* **359**, 1489–1494 (2018).
36. Xie, Y. *et al.* Boosting water dissociation kinetics on Pt-Ni nanowires by N-induced orbital tuning. *Adv. Mater.* **31**, 1807780 (2019).
37. Li, H. *et al.* Surface oxygen-mediated ultrathin PtRuM (Ni, Fe, and Co) nanowires boosting methanol oxidation reaction. *J. Mater. Chem. A* **8**, 2323–2330 (2020).
38. Chen, L. *et al.* Improved ethanol electrooxidation performance by shortening Pd-Ni active site distance in Pd-Ni-P nanocatalysts. *Nat. Commun.* **8**, 14136 (2017).
39. Huang, W. *et al.* Highly active and durable methanol oxidation electrocatalyst based on the synergy of platinum-nickel hydroxide-graphene. *Nat. Commun.* **6**, 10035 (2015).
40. Stewart, J. C. *et al.* First principles methods using CASTEP. *Z. Krist-Cryst. Mater.* **220**, 567–570 (2005).
41. Perdew, J. P., Burke, K. & Ernzerhof, M. Generalized gradient approximation made simple. *Phys. Rev. Lett.* **77**, 3865–3868 (1996).
42. Perdew, J. P. *et al.* Atoms, molecules, solids, and surfaces: Applications of the generalized gradient approximation for exchange and correlation. *Phys. Rev. B* **46**, 6671–6687 (1992).
43. Head, J. D. & Zerner, M. C. A Broyden-Fletcher-Goldfarb-Shanno optimization procedure for molecular geometries. *Chem. Phys. Lett.* **122**, 264–270 (1985).
44. Probert, M. I. J. & Payne, M. C. Improving the convergence of defect calculations in supercells: An ab initio study of the neutral silicon vacancy. *Phys. Rev. B* **67**, 075204 (2003).

Figures

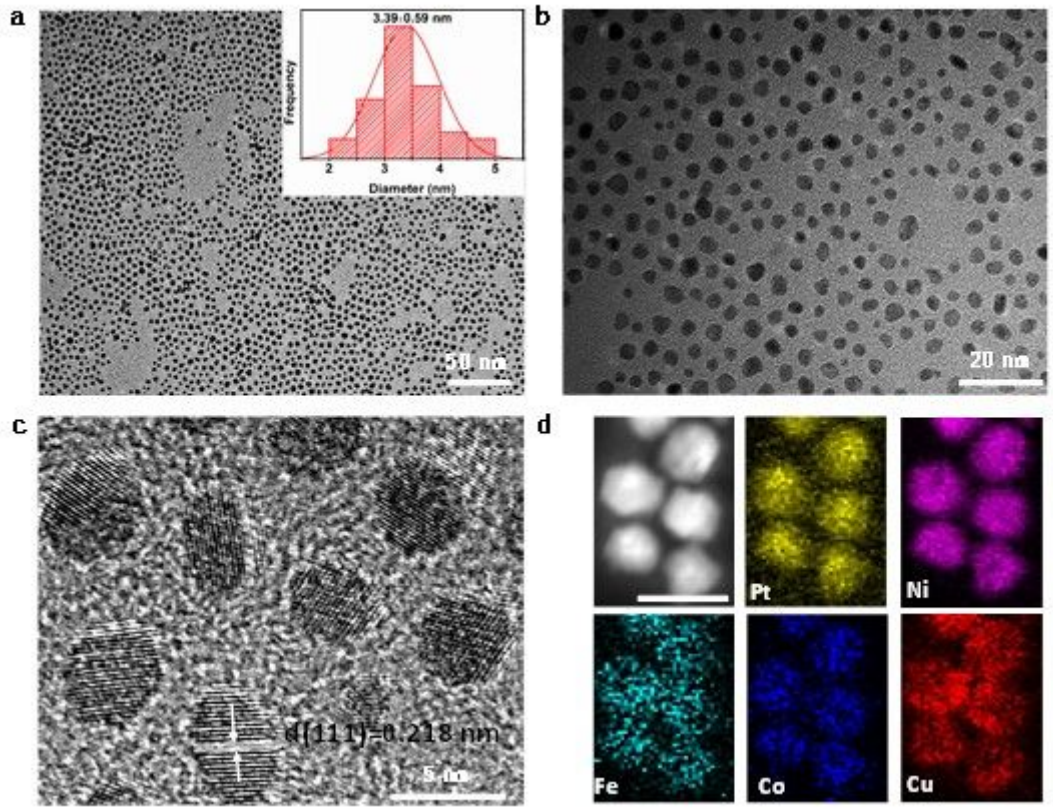

Figure 1

(a) and (b) TEM images, (c) HRTEM image and (d) the corresponding elemental mapping of Pt18Ni26Fe15Co14Cu27 NPs, scale bar, 5 nm.

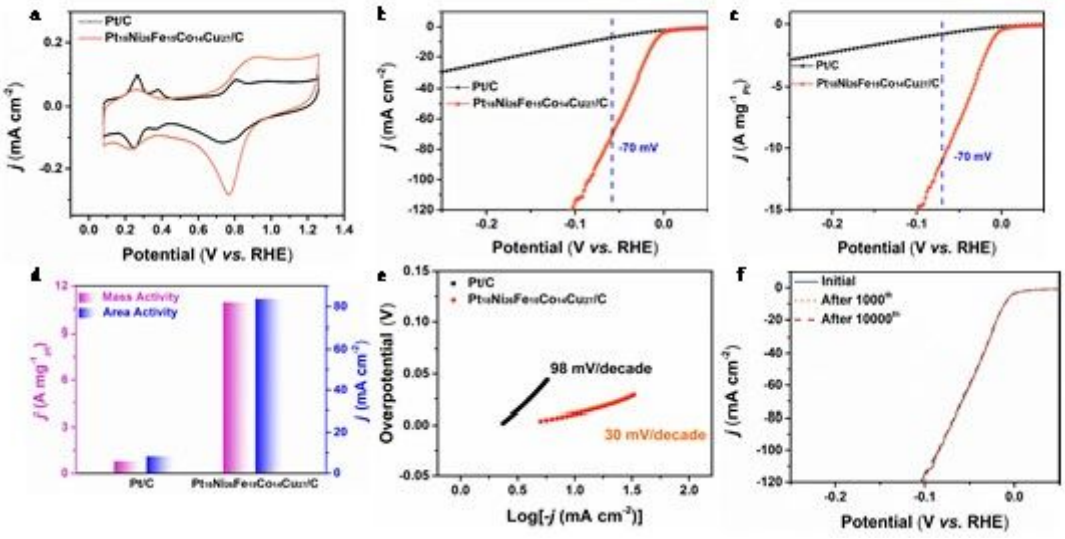

Figure 2

Electrocatalytic performance of the Pt18Ni26Fe15Co14Cu27/C and Pt/C for HER in 1 M KOH electrolyte. (a) CV curves. (b) HER polarization curves (geometrical area) and (c) Pt mass loading normalized (mass activity) LSV curves. (d) Comparison of area activity and mass activity values for HER at -70 mV vs. RHE.

(e) Tafel slope. (f) HER polarization curves (geometrical area) for Pt18Ni26Fe15Co14Cu27/C with different CV cycle

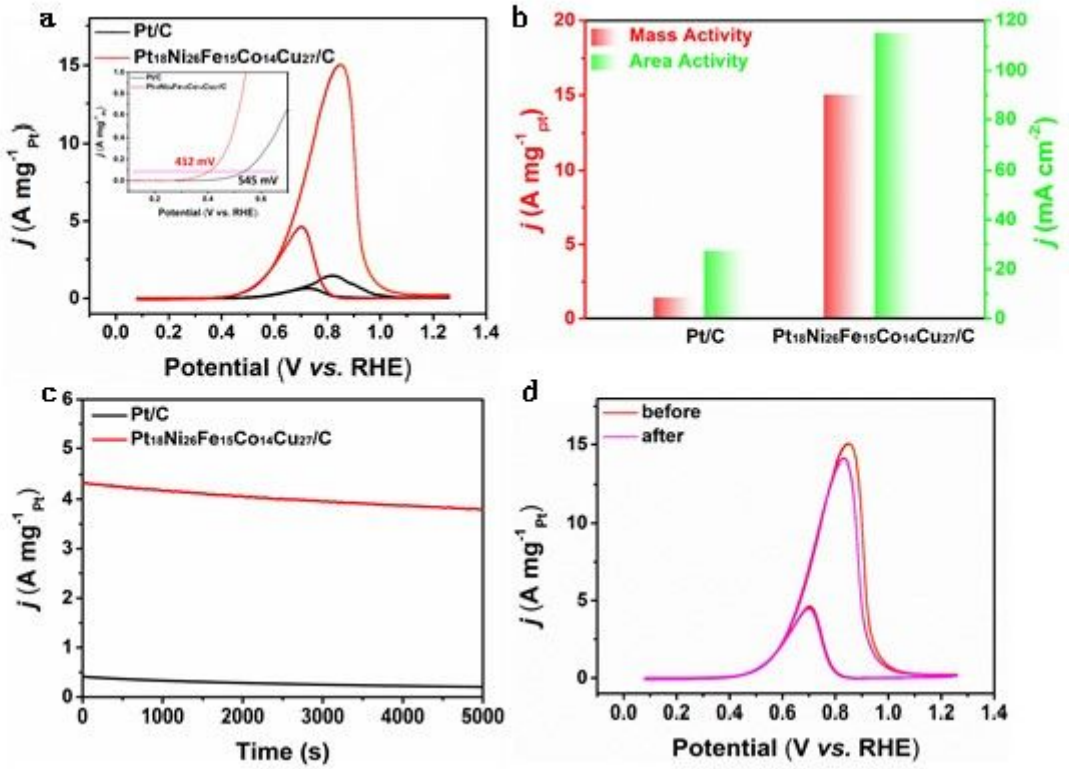

Figure 3

Methanol electro-oxidation performance of the Pt18Ni26Fe15Co14Cu27/C and Pt/C in 1 M KOH + 1 M CH3OH electrolyte. (a) CV curves, (the inset is the onset potential, the mass activity of 0.1 A mg-1pt) of Pt/C and Pt18Ni26Fe15Co14Cu27/C. (b) Peak values of mass activity and area activity. (c) Chronoamperometric tests for MOR at 0.65 V vs. RHE. (d) CV curves of the Pt18Ni26Fe15Co14Cu27/C before and after 1000 cycles.

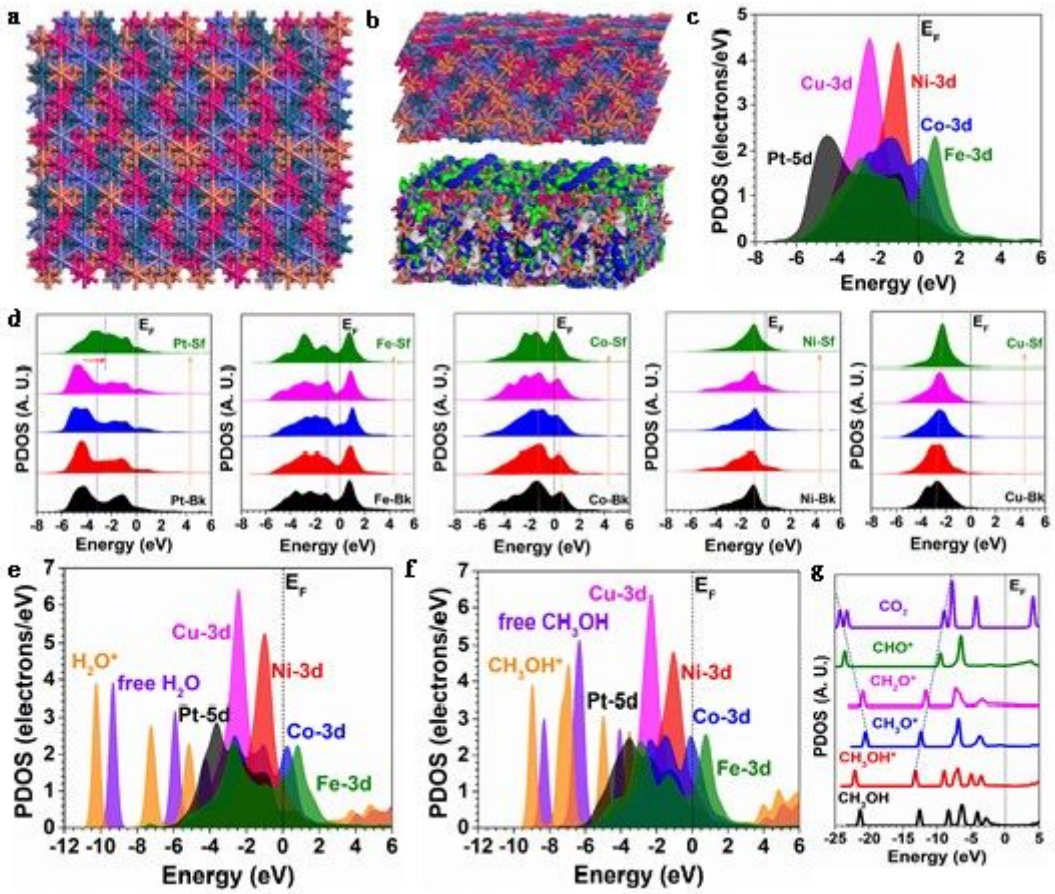

Figure 4

(a) The side view of the structural configuration of HEA. (b) The side view of HEA structural configuration and the real spatial contour plots for bonding and anti-bonding orbitals near EF. And the top view of the real spatial contour plots for bonding and anti-bonding orbitals near EF for the HEA. Dark green balls = Pt; Grey balls= Fe; Blue balls = Co; Pink balls = Ni and Orange balls = Cu. (c) The PDOSs of the HEA. (d) The site-dependent PDOSs of Pt, Fe, Co, Ni, and Cu in HEA. (e) The PDOSs for the water adsorption. (f) The PDOSs for the CH3OH adsorption. (g) The PDOSs for the key intermediates of MOR.

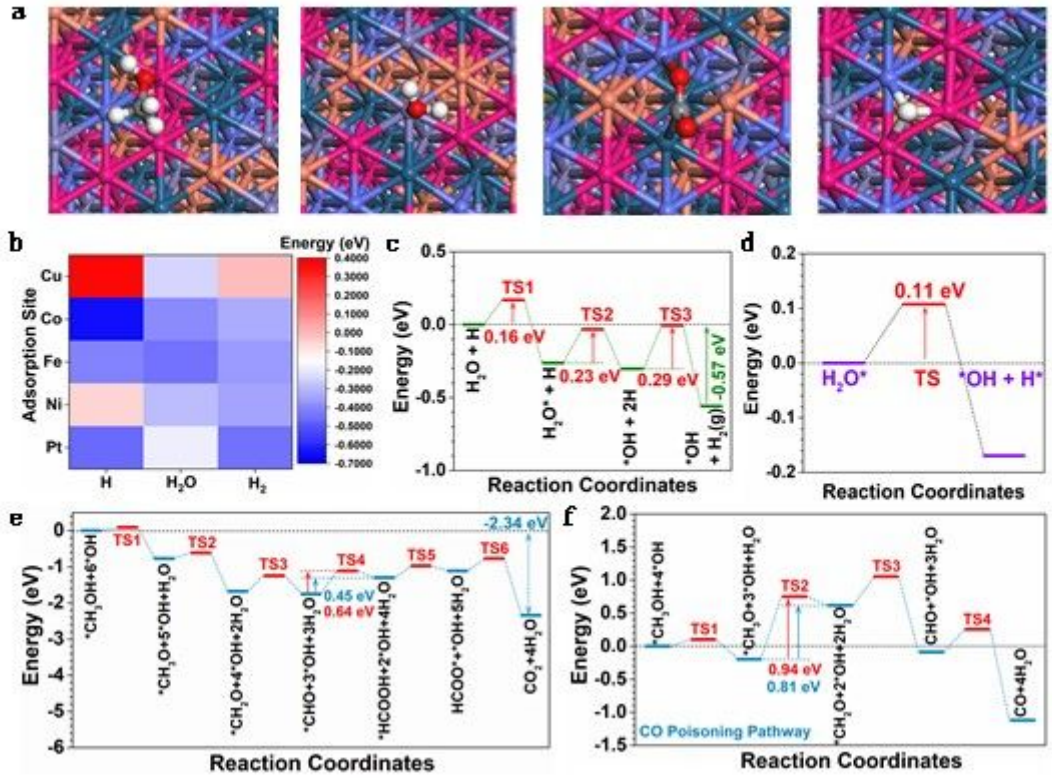

Figure 5

(a) The structural configuration of stable adsorption of key intermediates in HER and MOR. From left to right: CH3OH, H2O, CO2, H. Dark green balls = Pt; Grey balls= Fe; Blue balls = Co; Pink balls = Ni; Orange balls = Cu; Red balls= O and White balls = H. (b) The binding energy mapping of HER. (c) The energetic pathway of the alkaline HER. (d) The activation energies of water dissociation. (e) The energetic pathway of the alkaline MOR. (f) The energetic pathway of CO poisoning.

Supplementary Files

This is a list of supplementary files associated with this preprint. Click to download.

- SupportingInformation.doc